974 *Chem. Mater.* **2010,** *22,* 974–987
DOI:10.1021/cm901860y

CHEMISTRY OF MATERIALS
Article

Supercapacitor-Type Behavior of Carbon Composite and Replica Obtained from Hybrid Layered Double Hydroxide Active Container†

Thomas Stimpfling and Fabrice Leroux*

Laboratoire des Matériaux Inorganiques, UMR 6002-CNRS, Université Blaise Pascal, 24 av. des Landais, 63177 Aubière cedex, France

Received June 29, 2009. Revised Manuscript Received September 8, 2009

An original concept based on carbon replica method and adapted on organic/inorganic (O/I) hybrid layered double hydroxide (LDH) assembly is used to impart resulting carbon composites and replicas with interesting electrochemical properties. Thanks to the isomorphous cation substitution possible within the LDH layers, a series of O/I materials are prepared using the emulsifier 2-acrylamido-2-methyl-1-propanesulfonate acid (AMPS) as a source of carbon and Zn_2Al, $Co_2Al_{0.5}Fe_{0.5}$ and Ni_2Al as the LDH framework container. The process of carbonization and acid leaching is characterized by *in situ* X-ray diffractometry, Raman spectroscopy, and the pore formation of the resulting carbon replica by nitrogen adsorption. According to the carbonization/acid-leaching procedure, the electrochemical behavior is characterized in various aqueous electrolytes, using four salts, including 1.0 M $NaNO_3$, 0.5 M Na_2SO_4, 1 M Na_2SO_3, and 6 M KOH by means of cyclic voltammetry, galvanostatic mode, and complex impedance spectroscopy. Here, the key facet is the combination of the capacitive behavior of carbon, the pseudo-capacitive response coming from its functionalized surface, as well as redox reactions resulting from the inorganic particles present in the carbon composite and acting as a pore former during the acid leaching. From an optimized potential window of 1.2 V in 1 M Na_2SO_3, an electric energy of 11.0 W h/kg associated with a power density of 87.75 kW/kg is retrieved at a current density of 10 mA/g for carbon replica obtained from $Co_2Al_{0.5}Fe_{0.5}$/AMPS, and this is determined to be stable at moderate regime without significant capacitance fading. Meanwhile, a corresponding carbon composite, i.e., before acid leaching, presents over an optimized potential window of 1.8 V, a capacitance per surface unit of 92.6 μF/cm^2 at slow scan rate, largely because of the pseudo-capacitance effect, and a reversible redox reaction of 43 mAh/g is obtained at the C/3 regime in galvanostatic mode. Finally, preliminary tests in an asymmetric capacitor give some hints on the versatility of the new innovative approach using electrochemically active template, which creates the carbon part with suitable (pseudo)-capacitive properties, as well as being electronically conductive embedding inorganic redox centers.

1. Introduction

Complementary to lithium or lithium-ion batteries that provide high specific energy, electrochemical capacitors—so-called "supercapacitors"—have the potential to deliver high power density in a very short time, and they have excellent cyclability, thus explaining the renewed interest for such electrochemical devices in different domains such as digital telecommunication systems, uninterruptible power supplies for computers, and electric/hybrid vehicles. Supercapacitors can be divided into two types, according to the mechanisms involved in energy storage: either (i) superficial, so-called "electrochemical double-layer capacitors" (EDLCs), as illustrated by carbon materials,[1] or (ii) multielectron-transfer faradic reaction with fast charge discharge properties—the so-called "pseudo-capacitors" or redox-capacitors, as exemplified by metal oxides.[2]

As reported in the recent review devoted to carbon materials,[3] development to reach desired energy target implies further surface functionalization, and it is surmised that carbon composites are potentially of interest to combine a battery with a supercapacitor in one carbon-based system, or by blending hydrogen storage with fuel-cell functions in one integrated system. Indeed, carbon materials are known to be ubiquitous and are extensively studied in domain regarding negative electrode materials in lithium-ion batteries, supercapacitors, fuel cells, sensors, etc.; however, to fulfill many modern-day applications, new synthetic approaches are investigated to produce porous carbon materials with suitable properties.[4]

† Part of the 2010 "Materials Chemistry of Energy Conversion Special Issue".

*Author to whom correspondence should be addressed. Tel.: (+33) 473 407036. Fax: (+33) 473 407108. E-mail: Fabrice.Leroux@univ-bpclermont.fr.

(1) (a) Qu, D.; Shi, H. *J. Power Sources* **1998**, *74*, 99. (b) Frackowiak, E.; Beguin, F. *Carbon* **2001**, *39*, 937. (c) Gamby, J.; Taberna, P. L.; Simon, P.; Fauvarque, J. F.; Chesneau, M. *J. Power Sources* **2001**, *101*, 109.
(2) (a) Conway, B. E. *J. Electrochem. Soc.* **1991**, *138*, 1539. (b) Conway, B. E.; Briss, V.; Sarangapani, S.; Tilak, B. V.; Chen, C. P. *J. Electrochem. Soc.* **1996**, *143*, 3791. (c) Lee, H. Y.; Goodenough, J. B. *J. Solid State Chem.* **1999**, *144*, 220. (d) Wojtowicz, J. *J. Power Sources* **1997**, *66*, 1.
(3) Stein, A.; Wang, Z.; Fierke, M. A. *Adv. Mater.* **2009**, *21*, 265.
(4) Liang, C.; Li, Z.; Dai, S. *Angew. Chem., Int. Ed.* **2008**, *47*, 3696.

Published on Web 10/16/2009

To respond to these topical requirements and, more specifically, to those devoted to energy storage, special designs are developed to supply bulk and more importantly interfacial enhanced properties. Two major aspects govern the latter: an extended and hierarchically controlled surface area, and a multimodal porosity is here often whished for the transfer of migrating ions in tandem with wettability, as well as an adapted functionalization to reach electrochemical performance.

Porous carbon materials may be obtained through two major routes that were recently reviewed, both of which are based on template synthesis, using either a hard template or a soft template,[4] and the carbonization defined as the "thermal conversion" of organic materials to carbon[5] occurs in a confined space, usually after the removal of silica scaffolding. In the first category, one must remember the pioneering work of Knox and coworkers, using spherical solid silica gel as a template and the impregnation/infiltration of phenol-hexamine as the carbon precursor followed by polymerization, cross-linking, and carbonization of the organic component and finally dissolution of the silica template.[6] Even if the carbon materials are not ordered and the pore size distribution is often large, this route is still investigated using other colloidal crystal templates with different sources of carbon precursor such as sucrose,[7] poly(furfuryl alcohol),[8] or phenolic resin.[9] In this sacrificial hard-template approach, another aspect is to use a perfectly ordered inorganic structure to be converted into ordered microporous, mesoporous, or macroporous carbon materials, such as β-, L-,[10] Y-,[11] Na-Y-,[12] and EMC-2[13] zeolites, MCM-48,[14] SBA-1,[15] SBA-15,[16] and SBA-16[17] mesoporous silica, and a hollow macroporous sphere using core/shell structure.[18]

In the soft-template route, although successful in the synthesis of metal oxides, the alkyl-chain-based surfactant does not directly template the synthesis of mesoporous carbon and, therefore, should be removed before carbonization, as illustrated by pluronic (poly(ethylene oxide)−*b*-poly(propylene oxide)−*b*-poly(ethylene oxide) (PEO−PPO−PEO)) as the structure-directing agent with a mixture of phloroglucinol and formaldehyde as an inexpensive carbon source that may cause a particular shape, such as mesoporous carbon microwires and nanowires.[19] Blocks of copolymers are then preferred for the soft-template synthesis, because of their self-assembly possibility in fabricating versatile macromolecular architecture, and carbon nanostructures may be obtained from polystyrene−*b*-poly(4-vinylpyridine) (PS-P4 VP) and resorcinol and formaldehyde (RF) to obtain the highly cross-linked resin before carbonization,[20] as well as by pluronic with the same resin.[21] Similarly, triblock polymers are used to shape semigraphitized nanorod assemblies after cross-linking into the channels of SBA-15, carbonization followed by graphitization for which the transition metal is acting as a catalyst and, subsequently, is embedded, creating an ordered mesostructured carbon/metallic MoO_2.[22]

Concerning the functionalization (surface or bulk modification), the chemical modification is difficult, because of the low reactivity of carbon and, therefore, requires, for instance, strong oxidative treatment with oxygenated functionalities,[23] organic monomer,[24] or diazonium-based molecules, generated in situ,[25] reduced to yield sulfonic acid-containing aryl groups[26] or based on ionic liquid, the latter acting as a reactant and solvent.[27] Among the different functionalizations, impregnation with an organic monomer is believed to be a key advantage, because the resulting structure has the bifunctionality of mesoporous carbons and organic polymers,[4] and nanostructured organic materials are obtained from (i) a hard template (including silica nanoparticles, zeolites, periodic mesoporous silicas, and aluminum oxide membranes) or (ii) soft material such as colloidal crystal.[28]

In addition, as far as electrochemical conversion is concerned, the presence of electroactive centers is highly suitable. Considering the difficulty to functionalize the carbon surface, an enticing new concept is to use an active template process. Among other candidates, our interest in layered double hydroxide-type (LDH) materials in the preparation of carbon replica arises from their nanocontainer and nanoreactor aspects that are suitable for the sequestration of the organic molecule, and its further

(5) Lewis, I. C. *Carbon* **1982**, *20*, 519.
(6) Knox, J. H.; Kaur, B.; Millward, G. R. *J. Chromatogr.* **1986**, *352*, 3.
(7) Han, S.; Kim, M.; Hyeon, T. *Carbon* **2003**, *41*, 1525.
(8) Yao, J.; Wang, H.; Chan, K. Y.; Zhang, L.; Xu, N. *Microporous Mesoporous Mater.* **2005**, *82*, 183.
(9) Moriguchi, I.; Nakahara, F.; Furukawa, H.; Yamada, H.; Kudo, T. *Electrochem. Solid State Lett.* **2004**, *7*, A221.
(10) Kyotani, T.; Ma, Z. X.; Tomita, A. *Carbon* **2003**, *41*, 1451.
(11) Matsuoka, K.; Yamagishi, Y.; Yamazaki, T.; Setoyama, N.; Tomita, A.; Kyotani, T. *Carbon* **2005**, *43*, 876.
(12) Ania, C. O.; Khomenko, V.; Raymundo- Piñero, E.; Parra, J. B.; Beguin, F. *Adv. Funct. Mater.* **2007**, *17*, 1828.
(13) Gaslain, F. O. M.; Parmentier, J.; Valtchev, V. P.; Patarin, J. *Chem. Commun.* **2006**, 991.
(14) Ryoo, R.; Joo, S. H.; Jun, S. J. *J. Phys. Chem. B* **1999**, *103*, 7743.
(15) Ryoo, R.; Joo, S. H.; Kruk, M.; Jaroniec, M. *Adv. Mater.* **2001**, *13*, 677.
(16) (a) Joo, S. H.; Choi, S. J.; Oh, I.; Kwak, J.; Liu, Z.; Terasaki, O.; Ryoo, R. *Nature* **2001**, *412*, 169. (b) Zhang, W. H.; Liang, C.; Sun, H.; Shen, Z.; Guan, Y.; Ying, P.; Li, C. *Adv. Mater.* **2002**, *14*, 1776. (c) Lu, A.; Kiefer, A.; Schmidt, W.; Schüth, F. *Chem. Mater.* **2004**, *16*, 100.
(17) Fuertes, A. B.; Lota, G.; Centeno, T. A.; Frackowiak, E. *Electrochim. Acta* **2005**, *50*, 2799.
(18) Zhang, F. Q.; Meng, Y.; Gu, D.; Yan, Y.; Yu, C. Z.; Tu, B.; Zhao, D. Y. *J. Am. Chem. Soc.* **2005**, *127*, 13508.
(19) (a) Liang, C.; Dai, S. *J. Am. Chem. Soc.* **2006**, *128*, 5316. (b) Steinhart, M.; Liang, C.; Lynn, G. W.; Gösele, U.; Dai, S. *Chem. Mater.* **2007**, *19*, 2383.
(20) Liang, C.; Hong, K.; Guiochon, G. A.; Mays, J. W.; Dai, S. *Angew. Chem., Int. Ed.* **2004**, *43*, 5785.
(21) (a) Tanaka, S.; Nishiyama, Y.; Egashira, K.; Ueyama, K. *Chem. Commun.* **2005**, 2125. (b) Meng, Y.; Gu, D.; Zhang, F. Q.; Shi, Y. F.; Cheng, L.; Feng, D.; Wu, Z. X.; Chen, Z. X.; Wan, Y.; Stein, A.; Zhao, D. Y. *Chem. Mater.* **2006**, *18*, 4447.
(22) Ji, X.; Herle, P. S.; Rho, Y.; Nazar, L. F. *Chem. Mater.* **2007**, *19*, 374.
(23) Bahr, J. L.; Tour, J. M. *J. Mater. Chem.* **2002**, *12*, 1952.
(24) Choi, M.; Ryoo, R. *Nat. Mater.* **2003**, *2*, 473.
(25) Price, B. K.; Hudson, J. L.; Tour, J. M. *J. Am. Chem. Soc.* **2005**, *127*, 14867.
(26) Wang, X. Q.; Liu, R.; Waje, M. M.; Chen, Z. W.; Yan, Y. S.; Bozhilov, K. N.; Feng, P. Y. *Chem. Mater.* **2007**, *19*, 2395.
(27) Liang, C. D.; Huang, J. F.; Li, Z. J.; Luo, H. M.; Dai, S. *Eur. J. Org. Chem.* **2006**, 586.
(28) Thomas, A.; Goettmann, F.; Antonietti, M. *Chem. Mater.* **2008**, *20*, 738.

reaction in a confined environment, as well as their highly versatile chemical composition.[29] The LDH structure referred to the natural hydrotalcite is described with the ideal formula, $[M^{II}_{1-x}M^{III}_{x}(OH)_2]_{intra}[A_{x/m}{}^{m-}\cdot nH_2O]_{inter}$, where M^{II} and M^{III} are metal cations, A represents the anions, and the subscripts "intra" and "inter" denote the intralayer domain and the interlayer space, respectively. The structure consists of brucite-like layers constituted of edge-sharing $M(OH)_6$ octahedra. Partial M^{II} to M^{III} substitution induces a positive charge for the layers, balanced with the presence of the interlayered anions that are the carbon source here.

Inspired by some pioneering works to produce carbon replica adsorbents,[30] we reported the utilization of the LDH framework as a nanoreactor to produce the carbon replica, and we determined that an inorganic framework during the calcinations impedes the cross-linking reactions, thus forcing the carbon to develop large microporosity, and, in addition, the departure of inorganic byproduct creates the porosity at a mesoscale and/or macroscale, with the sacrificial inorganic template acting as a porogen agent.[31] From the styryl-based interleaved molecule and a "passive" LDH container, Zn_2Al, with a capacitance of 70−80 F/g, corresponding to 5−10 μF/cm^2 only, is obtained in H_2SO_4 (1 M), reaching the limitation of EDLC.[31c] To enhance the performance, we assume that the next step is to generate pseudo-capacitance from carbon, as well as from LDH sources.

The well-known key feature of using LDH as a single molecular precursor is to afford an uniform distribution of all metal cations on an atomic level; this concept has been used to produce nanoparticles of different cation compositions: vanadium and copper oxides;[32] mixed magnesium and vanadium oxides;[33] tetragonal $NiCr_2O_4$;[34] nanosized cobalt aluminate;[35] Ni,Al;[36] manganese-doped copper-based mixed oxides;[37] copper-based oxides;[38] copper, nickel, chromium mixed oxides;[39] chromium, copper, magnesium mixed oxides;[40] (Cu,Ni)Mg,Mn oxides;[41] Li, (Ni,Co) manganese-based spinel;[42] cobalt-based-LDH with aluminum, iron, gallium, and indium;[43] $CoFe_2O_4$[44] and $NiFe_2O_4$;[45] or $Ni_{1-x}Zn_xFe_2O_4$.[46] In conjunction to the fact that *in situ* polymerization is demonstrated for styryl-,[47] acrylate-,[48] or acrylamide-based[49] monomers, thus making a large number of possible O/I LDH assemblies to potentially generate carbon materials.

Here, an intralayer cation composition is assumed, considering the examples with LDH compounds as electrode materials and more specifically as a supercapacitor, while the choice of monomer surfactant is taken by the fact that nitrogen-containing carbon may supply pseudocapacitance to carbon.[12,50] Ni^{2+}-based LDH compounds are considered as an alternative electrode material for nickel batteries,[51] and large capacitance were reported either from electrochemically deposited nanostructured Co_xNi_{1-x} LDH,[52] Cobalt-based LDH materials prepared by separate nucleation and aging steps[53] or from hybrid materials where interleaved molecules such as benzoate prevent the collapse of the layer structure, consequently permitting LDH materials to be reconstructed by rehydration and, thus, yield to high capacitance.[54]

In this work, we have attempted to validate an original concept using three different LDH frameworks that should induce whether or not electrochemically active thermal byproducts, such as Zn_2Al, $Co_2Fe_{0.5}Al_{0.5}$, and Ni_2Al, are formed. The carbon source is a linear *in situ*

(29) Leroux, F.; Taviot-Guého, C. *J. Mater. Chem.* **2005**, *15*, 3628.
(30) (a) Putyera, K.; Bandosz, T. J.; Jagiello, J.; Schwarz, J. A. *Clays Clay Sci.* **1994**, *42*, 1. (b) Putyera, K.; Bandosz, T. J.; Jagiello, J.; Schwarz, J. A. *Appl. Clay Sci.* **1995**, *10*, 177. (c) Bandosz, T.; Jagiello, J.; Putyera, K.; Schwarz, J. A. *Chem. Mater.* **1996**, *8*, 2023–2029. (d) Putyera, K.; Bandosz, T. J.; Jagiello, J.; Schwarz, J. A. *Carbon* **1996**, *34*, 1559.
(31) (a) Leroux, F.; Raymundo-Piñero, E.; Nedelec, J. M.; Beguin, F. *J. Mater. Chem.* **2006**, *16*, 2074. (b) Leroux, F.; Dubois, M. *J. Mater. Chem.* **2006**, *16*, 4510. (c) Dielectric present capacitance C (F/cm^2)= $(\varepsilon_0\varepsilon_r)/e$ (ε_0=8.85 × 10^{-14}, with ε_5 of the order of 10, and separation of 10 μm) of the order of 10^{-3} μF/cm^2, while EDLC may supply 10−20 μF/cm^2, which is four orders of magnitude greater than that of dielectric devices.
(32) Carja, G.; Niiyama, H. *Mater. Lett.* **2005**, *59*, 3078–3080.
(33) Holgado, M. J.; San Roman, S.; Malet, P.; Rives, V. *Mater. Chem. Phys.* **2005**, *89*, 49–55.
(34) Sileo, E. E.; Jobbagy, M.; Paiva-Santos, C. O.; Regazzoni, A. E. *J. Phys. Chem. B* **2005**, *109*, 10137–10141.
(35) Chen, Z.; Shi, E.; Li, W.; Zheng, Y.; Zhu, Q.; Zhuang, J.; Xiao, B.; Tang, L. *Mater. Sci. Eng., B* **2004**, *B107*, 217–223.
(36) (a) Mikulova, Z.; Cuba, P.; Balabanova, J.; Rojka, T.; Kovanda, F.; Jiratova, K. *Chem. Pap.* **2007**, *61*, 103–109. (b) Qi, C.; Amphlett, J. C.; Peppley, B. A. *Appl. Catal., A* **2006**, *302*, 237–243.
(37) Li, F.; Zhang, L.; Evans, D. G.; Duan, X. *Colloids Surf., A* **2004**, *244*, 169–177.
(38) (a) Barrault, J.; Derouault, A.; Courtois, G.; Maissant, J. M.; Dupin, J. C.; Guimon, C.; Martinez, H.; Dumitriu, E. *Appl. Catal., A* **2004**, *262*, 43–51. (b) Zhang, L.; Li, F.; Evans, D. G.; Duan, X. *Mater. Chem. Phys.* **2004**, *87*, 402–410.
(39) Zhang, L.; Zhu, J.; Jiang, X.; Evans, D. G.; Li, F. *J. Phys. Chem. Solids* **2006**, *67*, 1678–1686.
(40) Crivello, M.; Perez, C.; Fernandez, J.; Eimer, G.; Herrero, E.; Casuscelli, S.; Rodriguez-Castellon, E. *Appl. Catal., A* **2007**, *317*, 11–19.
(41) Kovanda, F.; Grygar, T.; Dornicak, V.; Rojka, T.; Bezdicka, P.; Jiratova, K. *Appl. Clay Sci.* **2005**, *28*, 121–136.
(42) (a) Lu, Y.; Wei, M.; Yang, L.; Li, C. *J. Solid State Chem.* **2007**, *180*, 1775–1782. (b) Zhang, X.; Wen, Z.; Zhu, X.; Lin, B.; Zhang, J.; Huang, S. *Mater. Lett.* **2006**, *60*, 1470–1474.
(43) Radha, A. V.; Thomas, G. S.; Kamath, P. V.; Shivakumara, C. *J. Phys. Chem. B* **2007**, *111*, 3384–3390.
(44) Manova, E.; Kunev, B.; Paneva, D.; Mitov, I.; Petrov, L.; Estournes, C.; D'Orleans, C.; Rehspringer, J.-L.; Kurmoo, M. *Chem. Mater.* **2004**, *16*, 5689–5696.
(45) (a) Li, X. D.; Yang, W. S.; Li, F.; Evans, D. G.; Duan, X. *J. Phys. Chem. Solids* **2006**, *67*, 1286–1290. (b) Ruano-Casero, R. J.; Perez-Bernal, M. E.; Rives, V. *Z. Anorg. Allg. Chem.* **2005**, *631*, 2142–2150.
(46) (a) Li, F.; Liu, X.; Yang, Q.; Liu, J.; Evans, D. G.; Duan, X. *Mater. Res. Bull.* **2005**, *40*, 1244–1255. (b) Meng, W.; Li, F.; Evans, D. G.; Duan, X. *J. Porous Mater.* **2004**, *11*, 97–105.
(47) (a) Vieille, L.; Taviot-Guého, C.; Besse, J.-P.; Leroux, F. *Chem. Mater.* **2003**, *15*, 4369–4376. (b) Moujahid, E. M.; Besse, J.-P.; Leroux, F. *J. Mater. Chem.* **2002**, *12*, 3324 –3330.
(48) (a) Vaysse, C.; Guerlou-Demourgues, L.; Duguet, E.; Delmas, C. *Inorg. Chem.* **2003**, *42*, 4559. (b) Aguzzi, A.; Ambrogi, V.; Costantino, U.; Marmottini, F. *J. Phys. Chem. Solids* **2007**, *68*, 808. (c) Roland-Swanson, C.; Besse, J.-P.; Leroux, F. *Chem. Mater.* **2004**, *16*, 5512.
(49) (a) Itoh, T.; Yamashita, M.; Shichi, T.; Yui, T.; Takagi, K. *Chem. Lett.* **2005**, *34*, 990–991. (b) Itoh, T.; Shichi, T.; Yui, T.; Takagi, K. *Langmuir* **2005**, *21*, 3217–3220.
(50) Frackowiak, E.; Lota, G.; Machnikowski, J.; Vix-Guterl, C.; Beguin, F. *Electrochim. Acta* **2006**, *51*, 2209.
(51) (a) Roto, R.; Villemure, G. *J. Electroanal. Chem.* **2007**, *112*, 601. (b) Scavetta, E.; Ballarin, B.; Berettoni, M.; Carpani, I.; Giorgetti, M.; Tonelli, D. *Electrochim. Acta* **2006**, *51*, 2129.
(52) Gupta, V.; Gupta, S.; Miura, N. *J. Power Sources* **2008**, *175*, 680.
(53) Wang, Y.; Yang, W.; Zhang, S.; Evans, D. G.; Duan, X. *J. Electrochem. Soc.* **2005**, *152*, A2130.
(54) Su, L. H.; Zhang, X. G. *J. Power Sources* **2007**, *172*, 999.

polymerizable emulsifier 2-acrylamido-2-methyl-1-propanesulfonate acid (AMPS), and it is commercially produced as ion-exchange resin, flocculants, dispersants, adhesive, and thickeners. As previously mentioned, our idea is to use thermal LDH byproduct as a porogen agent to texture the resulting carbon replica,[31a,b] but also to study the electrochemical behavior of the composite formed by nanostructured inorganic phases embedded into a carbon matrix (i.e., before the acid-leaching step). The carbonization of these O/I LDH assemblies is characterized via *in situ* XRD, and the resulting carbon materials are characterized by electron spin resonance (ESR), Raman spectroscopy, N_2 adsorption, and direct observation of their textural morphologies by scanning electron microscopy (SEM). The capacitive properties are evaluated by means of potentiostatic and galvanostatic techniques, as well as by complex impedance spectroscopy, in different aqueous electrolytes ($NaNO_3$, Na_2SO_4, Na_2SO_3, and KOH) to compare the electrochemical double-layer formation (EDLC), to emphasize the pseudocapacitive phenomena and the possible much-slower redox reactions that are occurring simultaneously or at different regimes of cycling.

2. Experimental Section

2.1. Preparation of the Samples. $ZnCl_2$ (Acros), $AlCl_3 \cdot 6H_2O$ (Acros), $Ni(NO_3)_2 \cdot 6H_2O$ (Acros), $Al(NO_3)_3 \cdot 9H_2O$ (Acros), $Co(NO_3)_2 \cdot 6H_2O$ (Acros), $Fe(NO_3)_3 \cdot 9H_2O$ (Acros), 2-acrylamido-2-methyl-1-propanesulfonate acid (AMPS) (Aldrich), and NaOH (Aldrich) were used as received.

The hydrotalcite-like materials were prepared via the conventional coprecipitation method, and three resulting LDH phases (Zn_2Al/Cl, Ni_2Al/NO_3, and $Co_2Fe_{0.5}Al_{0.5}/NO_3$) were then used as precursors for the anion exchange reaction with AMPS. Experimentally, 250 mL of a solution of the salts M^{II} and M^{III} with a M^{II}/M^{III} ratio of 2 was added dropwise to distilled water under a nitrogen atmosphere, to avoid the carbonate contamination from air. The solution of salts was added at a constant flow of 2.0 mL/min. The pH was kept constant, via the addition of a solution of NaOH, at pH 8 ± 0.1, 10 ± 0.1, and 8 ± 0.1 for the Zn_2Al/Cl, Ni_2Al/NO_3, and $Co_2Fe_{0.5}Al_{0.5}/NO_3$ LDH phases, respectively. The slurries were then aged for three days, centrifuged, and finally washed several times with distilled water.

2.1.1. The O/I Hybrid LDH Phases. The hybrid LDH phases were prepared via an exchange reaction from the parent LDH slurries (the content of water was calculated from thermal treatment). Two solutions were prepared: one of 100 mL that contained LDH slurry maintained under a nitrogen atmosphere and another of 100 mL with the emulsifier AMPS. In each case, the quantity of AMPS was optimized to complete a full anion exchange reaction, and an amount of AMPS as high as 12, 10, and 15 times the anion exchange capacity of the precursor was used for Zn_2Al/Cl, Ni_2Al/NO_3, and $Co_2Fe_{0.5}Al_{0.5}/NO_3$, respectively. The pH was fixed at 7.0 ± 0.1 during the exchange reaction that was left for 3 days under a nitrogen atmosphere and vigorous stirring. The resulting O/I LDH slurries were centrifuged, washed several times with distilled water, and finally dried overnight at 30 °C.

The LDH phases $M^{II}_2M^{III}(OH)_6A^{m-} \cdot nH_2O$ will be denoted as $M^{II}_2M^{III}/A$ in the following discussion, with A being either Cl and NO_3 for the precursors or AMPS for the O/I LDH assemblies. Elemental analysis (N, S, Zn, Co, Ni, Fe, and Al) was performed at the Vernaison Analysis Center of CNRS, using inductively coupled plasma coupled with atomic emission spectroscopy (ICP/AES). Elemental analysis calculated from the experimental data is consistent with what should be expected from an LDH nominal composition (SEI-1).

2.1.2. Carbonization and Acid-Leaching Procedures. Pyrolysis of the hybrid LDH phases was performed in a tubular furnace under a constant nitrogen gas flow (120 mL/min). The samples were treated either at 500 or 600 °C (optimized temperatures obtained from *in situ* XRD measurement; see the Results and Discussion section) for 4 h (heating rate of 5 °C/min), then cooled at room temperature. The acid-leaching process was performed in HCl (concentration of 5 mol/L) for 3 days to dissolve the inorganic moiety. Indeed, depending of the temperature, different residual phases were identified after the carbonization process and for some of them, the HCl concentration (1 M) was not sufficient to provoke their dissolution. Therefore, 5 M HCl was then used. The obtained black powders were washed several times with decarbonated water. Hereafter, the carbon composites are called C-LDH-T and carbon replicas are called C-LDH-Td: material coming from carbonization at 500 °C of Zn_2Al/AMPS will be called C−Zn_2Al-500, and its derivative after demineralization will be called C−Zn_2Al-500d (in the absence of LDH sequestration for the organic molecule, C-AMPS-T and C-AMPS-Td, respectively).

2.2. Techniques of Characterization. *2.2.1. Powder X-ray Diffraction (XRD).* XRD profiles were obtained with a Siemens Model D500 X-ray diffractometer with a diffracted beam monochromator Cu Kα source. Patterns were recorded over the 2θ range of 2°−70°, in steps of 0.08° with a count time of 4 s.

2.2.1.1. XRD in Temperature. X-ray patterns were recorded by a Philips Model X'Pert Pro diffractometer that used Cu Kα radiation and was equipped with an Anton Paar Model HTK 16 chamber and RTMS detector. *In situ* temperature XRD measurements were conducted under a nitrogen atmosphere with a temperature holding time of 10 min between each measurement (using a heating rate of 1 °C/s). Scans were performed over the 2θ range of 3°−70°, in steps of 0.0334° with a count time of 180 s.

2.2.2. Raman Spectroscopy. Raman spectra were recorded in the backscattering geometry on a Jobin−Yvon Horiba Model T64000 spectrometer that was equipped with a liquid-nitrogen-cooled CCD detector. The excitation beam is provided by the 514.5 nm line of an argon-ion laser (Spectra Physics, Model 2017). The laser beam (~1 μm^2) is focused on the sample through an Olympus confocal microscope with 100× magnification. The measured power at the sample level was kept low, to avoid any damage of the material. A motorized three-axis stage and direct imaging allowed zones to be selected. Several Raman spectra have been recorded for each sample. The spectra have been corrected from the baseline, and deconvoluted using two Gaussian lines in the 800−2000 cm^{-1} spectral region.

2.2.3. Nitrogen Adsorption. A Micromeritics Model ASAP 2020 system was used for the nitrogen adsorption/desorption measurements at 77 K. The samples were outgassed under vacuum, initially at 150 °C for 2 h then at 350 °C for 46 h. The specific surface area was calculated from the BET and *t*-plot methods.

2.2.4. Electrochemistry. 2.2.4.1. Preparation of the Electrode and the Cell. The electrodes were obtained by mixing active material (80%), acetylene black (10%), and poly(vinylidene fluoride) (PVDF) (10%) in ethanol. Both electrodes of comparable mass (in the range of 0.3−2.5 mg) were deposited on

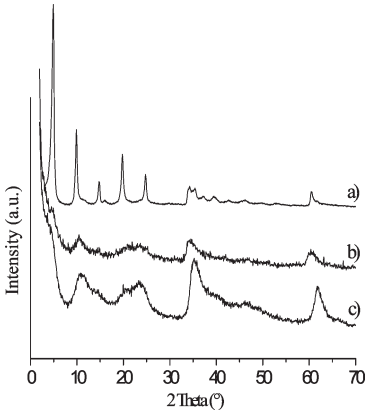

Figure 1. X-ray patterns of the O/I hybrid LDH materials: (a) Zn_2Al/AMPS, (b) $Co_2Fe_{0.5}Al_{0.5}$/AMPS, and (c) Ni_2Al/AMPS.

stainless steel 316 L disk (diameter of 12 mm) and electrically isolated between each other by a glassy fibrous separator used as an electrolyte reservoir. The materials were tested in symmetric two-electrode capacitors using a stainless steel Swagelok cell, the inner tube was isolated by a polypropylene membrane. An asymmetric electrochemical cell was used; negative and positive electrode materials were then different.

2.2.4.2. Electrochemical Testing. Aqueous electrolyte was prepared using four different salts: $NaNO_3$ (1.0 mol/L, pH 6.8, Acros), Na_2SO_4 (0.5 mol/L, pH 7.0, Acros), Na_2SO_3 (1.0 mol/L, pH 9.7, Prolabo), and KOH (6.0 mol/L, pH 14.0, Acros). The electrochemical characterizations were performed via cyclic voltammetry with a VSP multichannel potentiostat/galvanostat from BioLogic, using the EC-Lab V9.4 software. In each case, the voltammograms were recorded with several potential ranges according to the stability of the electrochemical response (electrolyte and materials). The scan rates were 2, 5, 10, 50, and 100 mV/s. The capacitance was calculated from the recorded current (I) value reported to the mass m of the active mass (I given in units of A/g) in the investigated potential domain divided by the sweep rate value (dV/dt, in units of V/s), following the formula $C = 2I_c/dV/dt$ given in units of A s/(V g) ($\equiv$ F/g), where I_c is the intensity measured during the cathodic sweep, and dV/dt is the potential step. For the galvanostatic mode (constant current), the electrode materials were cycled within the optimized potential domain ΔV. In this case, $C = 2I(dt/dV)_{exp}$where I is a constant current (expressed in units of A/g) and $(dt/dV)_{exp}$ is the experimental slope of the $t-V$ curve. The $I-V$ profile for acetylene black deposited on a stainless steel electrode was determined for the tested electrolytes with small capacitances (< 2 F/g). Complex impedance spectroscopy was performed on the electrochemical cell at a fixed potential imposed 5 minutes before applying a peak-to-peak amplitude of 20 mV and a frequency domain from 5 mHz to 200 kHz. Capacitance may be calculated by $C = 1/2\pi fZ''$where f is the frequency and Z'' the imaginary part of the complex impedance. The electrical energy and power density were calculated according to $E = {}^1/_2CV^2$ (F/(g V)$^2 \equiv$ A V^{-1} s V^2/g $\equiv$ W s/g $\equiv$ W h/kg) and$P = V^2/4 \times \mathrm{ESR} \times M$ expressed in units of V^2/(Ω g) ($\equiv$ V^2 V^{-1} A g$^{-1} \equiv$ W/kg), where ESR and M are the equivalent serial resistance measured on the $Z'-jZ''$ Nyquist curve and the mass of both electrode materials, respectively.

2.2.5. Scanning Electron Microscopy. Scanning electron microscopy (SEM) images were obtained on a Zeiss Model Supra 55 VP electron microscope at an accelerating voltage of 3 kV (at Casimir, Clermont-Ferrand, France).

Table 1. Structural Data, Cell Parameters, and Identification and Stability of the Thermal Products Generated by Calcinations under a Nitrogen Atmosphere

number of water molecules, nH$_2$O	Lattice Parameters				
	a (±0.01 nm)	c (±0.03 nm)	T_s (°C)[a]	by-product	formation temperature (°C)
			Zn_2Al/AMPS		
3.16	0.31	5.38	300	$ZnAl_2S_4$[b]	(500−800)[b]
				ZnO[c]	500[c]
				ZnS[c]	600[c]
				$ZnAl_2O_4$[c]	700[c]
			Ni_2Al/AMPS		
3.50	0.30	5.66	400	NiS[b]	(400−700)[b]
				Ni[c]	500[c]
				NiO[b]	(500−700)[b]
				NiO[d]	
				$NiAl_2O_4$[c]	800[c]
				Ni_3S_2[d]	
			$Co_2Fe_{0.5}Al_{0.5}$/AMPS		
3.16	0.31	5.71	300	Co[b]	(500−800)[b]
				CoO[c]	600[c]
				Co[d]	
				$FeAl_2O_4$[b]	(500−800)[b]
				Co_8FeS_8[b]	(500−800)[b]
				$CoFe_2O_4$[c]	600[c]
				Fe[b]	(600−900)[b]
				$FeAl_2O_4$[d]	

[a] T_s is the temperature limit of LDH framework stability. [b] Identified phase is present during the heating process and associated with their stability domain in temperature (°C). [c] By-product is stable in cooling and associated with their formation temperature (°C). [d] Phase crystallizes during the cooling.

3. Results and Discussion

3.1. Incorporation of the Surface Active Monomer. Pristine LDH phases, Zn_2Al/Cl, Ni_2Al/NO_3, and $Co_2Fe_{0.5}Al_{0.5}/NO_3$ are obtained via direct coprecipitation. Their associated XRD patterns exhibit diffraction lines typical of an LDH structure, which is generally described in $R\bar{3}m$ rhombohedral symmetry (SEI-2). The cell parameters a and c are calculated from the positions of the diffraction lines. The anion exchange reaction by AMPS induces an increase in the basal spacing ($d_{(003)}$) of the host structure (see Figure 1), in agreement with the literature.[55] The O/I hybrid LDH assemblies present some differences in crystallinity; Zn_2Al/AMPS is well-crystallized, whereas the two other phases present ill-defined diffraction peaks (the (00l) lines are then broad, showing that the coherence length along the stacking direction is rather small in the case of $Co_2Al_{0.5}Fe_{0.5}$/AMPS and Ni_2Al/AMPS). However, the exchange anion reaction is topotactic in the three cases, because the cell parameter a ($a = 2 \times d_{(110)}$), which is related to the position of the diffraction line (110), still remains at a constant value. The structural data are summarized in Table 1. The quantity of H_2O either as weakly sorbed or located in the interlamellar domain was evaluated by thermogravimetric analysis (TGA) (SEI-3).

3.2. Behavior in Temperature of the Hybrid LDH Phases under N_2. Powder XRD patterns recorded *in situ*

(55) Hussein, M. Z.; Seng, H. K. *J. Mater. Sci.* **2001**, *20*, 1787.

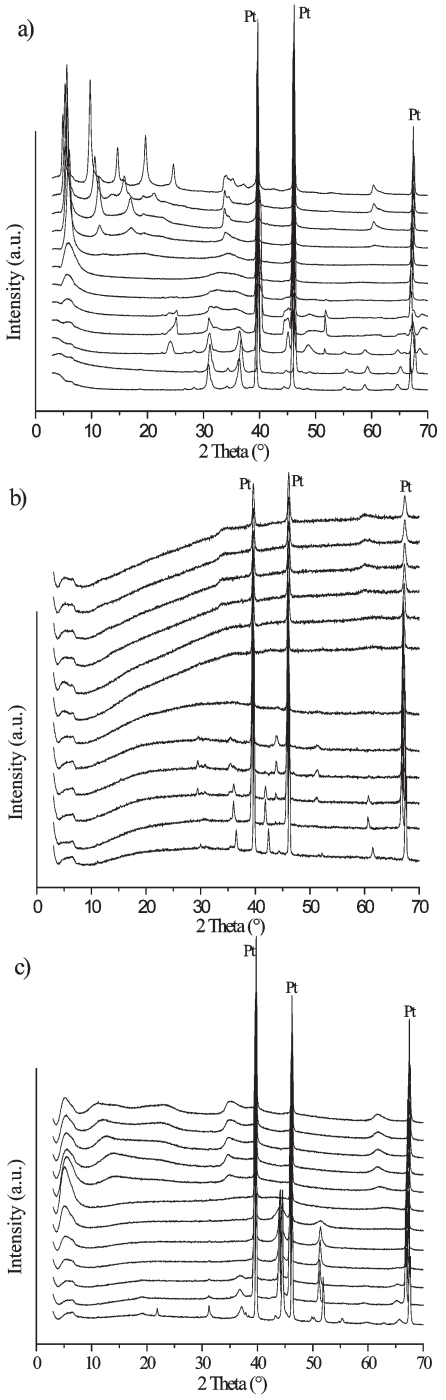

Figure 2. *In situ* XRD of (a) Zn_2Al/AMPS, (b) $Co_2Fe_{0.5}Al_{0.5}$/AMPS, and (c) Ni_2Al/AMPS under a nitrogen atmosphere. From top to bottom, $T = 25$ °C, 50 °C, 100 °C, ..., every 100 °C up to 900 °C, and back to 25 °C. The diagrams are shifted along the *y*-axis for clarity.

under a nitrogen atmosphere (see Figure 2) provide information about the stability and subsequent lamellar breakdown of the O/I LDH phase, as well as the nature, crystallinity, and formation of the resulting thermal byproduct. Indeed, the temperature of carbonization should correspond to the thermal treatment that leads to a XRD pattern that has as little peak intensity possible. In other words, the temperature should be higher than that observed for LDH framework breakdown and be lower than that corresponding to the crystallization of the byproduct.

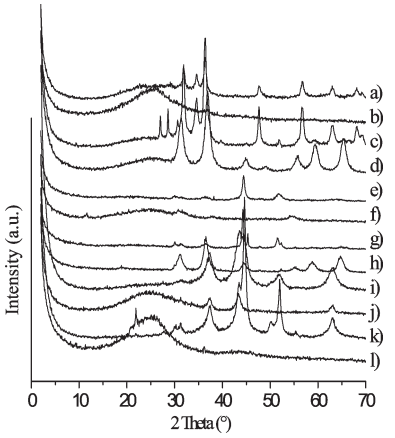

Figure 3. XRD patterns, after carbonization/acid-leaching procedures, of (a) C−Zn_2Al-500, (b) C−Zn_2Al-500d, (c) C−Zn_2Al-600, (d) C−Zn_2Al-600d, (e) C−$Co_2Fe_{0.5}Al_{0.5}$-500, (f) C−$Co_2Fe_{0.5}Al_{0.5}$-500d, (g) C−$Co_2Fe_{0.5}Al_{0.5}$-600, (h) C−$Co_2Fe_{0.5}Al_{0.5}$-600d, (i) C−Ni_2Al-500, (j) C−Ni_2Al-500d, (k) C−Ni_2Al-600, and (l) C−Ni_2Al-600d. The diagrams are shifted along the *y*-axis for clarity.

When treated at temperatures up to 300 or 400 °C (depending of the inorganic framework), a shift of the (00*l*) diffraction lines to larger 2θ values is progressively observed; this occurs in association with a decrease in the peak intensity. Such well-known phenomena correspond to the contraction of the lamellar gap, which is due to the loss of the interleaved water molecules and to a progressive amorphization. Consequently, at ∼500−600 °C, the XRD patterns are flat and inorganic byproducts start to crystallize. The nature of the byproduct is identified (Table 1). One should have in mind that *in situ* treatment up to 900 °C allows the observation of some metastable phases unstable when cooling at room temperature. This is the case for $ZnAl_2S_4$ (JCPDS File Card No. 89-4210), NiS (JCPDS File Card No. 1-1286), NiO (JCPDS File Card No. 22-1189), Co_8FeS_8 (JCPDS File Card No. 29-0484), while other inorganic phases are stable when formed such as ZnS (JCPDS File Card No. 5-0492), ZnO (JCPDS File Card No. 36-1451), $ZnAl_2O_4$ (JCPDS File Card No. 5-0669), Ni (JCPDS File Card No. 1-1260), $NiAl_2O_4$ (JCPDS File Card No. 10-0339), CoO (JCPDS File Card No. 9-0402), and $CoFe_2O_4$ (JCPDS File Card No. 22-1086) and that other phases are formed when cooling (see Table 1). The transformation of LDH to spinel is well-documented, and even its associated nanostructuration with the formation of nanoplatelets and nanorods has been recently reported.[56] However, because of the sulfonate function and the treatment under nitrogen, rather unusual phases are here formed, especially some sulfides, some of which have already been reported, such as ZnS,[57] because the Zn_2Al LDH framework is commonly used. One must note that the carbonization of such an O/I LDH framework induces a reduction of the metal cation ($Fe^{III} \rightarrow Fe^{II}$, $Co^{II} \rightarrow Co^0$, and $Ni^{II} \rightarrow Ni^0$), even under inert atmosphere.

(56) Sun, G.; Sun, L.; Wen, H.; Jia, Z.; Huang, K.; Hu, C. *J. Phys. Chem. B* **2006**, *110*, 13375.
(57) Moujahid, E. M.; Besse, J.-P.; Leroux, F. *J. Mater. Chem.* **2003**, *13*, 258–264.

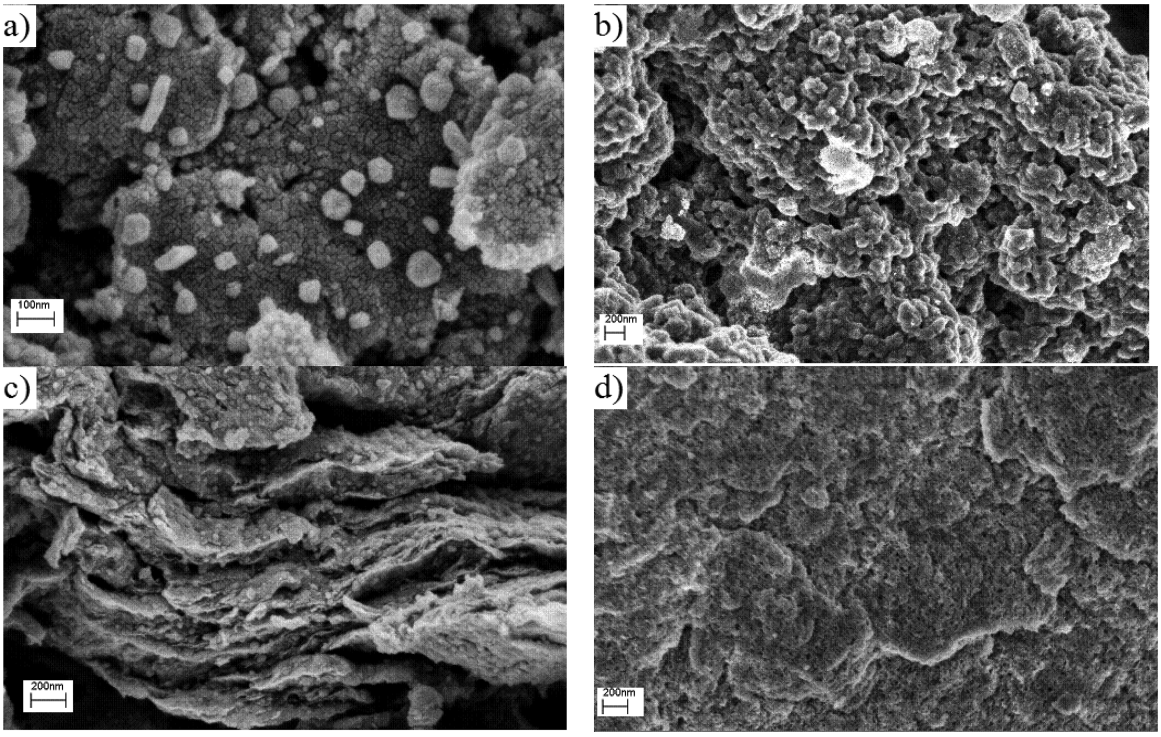

Figure 4. Selective SEM pictures for (a) C−Ni_2Al-600, (b) C−Ni_2Al-500d, (c) C−$Co_2Fe_{0.5}Al_{0.5}$-500, and (d) C−$Co_2Fe_{0.5}Al_{0.5}$-600d.

Table 2. Textural and Electrochemical Data, as a Function of the Carbonization Temperature and Acid-Leaching Procedure

		BET (*t*-plot)			Na_2SO_4 (0.5 mol/L)				$NaNO_3$ (1 mol/L)			
parameter	D/G L_a (nm)[a]	S[b] (m^2/g)	S_μ[b] (m^2/g)	S_T[b] (m^2/g)	C[c] (F/g)	C[c] [μF/cm^2]	q_0*[d] (C/g)	q_t*[e] (C/g)	C[c] (F/g)	C[c] [μF/cm^2]	q_0*[d] (C/g)	q_t*[e] (C/g)
C-AMPS-500	4.63				6		3	13	9		4	20
C-AMPS-500d	5.31	102#			2	2	1	4	9.5	9	3	31
C-AMPS-600	5.34				4		2	5	5		1	29
C-AMPS-600d	5.73	43#			3	7	0.5	14	7	16	2	20
C−Zn_2Al-500	7.66	57#			2	4	0.5	7	3	5	2	4.5
C−Zn_2Al-500d	4.37	396	154	243	6	1.5	1	31	6	1.5	0	137
C−Zn_2Al-600	6.33	31#			2	6	1	26	2	6	1	3
C−Zn_2Al-600d	4.81	170	86	85	24	14	17	25	24	14	11	50
C−$Co_2Fe_{0.5}Al_{0.5}$-500	5.58	95#			28	29.5	8	30	38	40	10	43
C−$Co_2Fe_{0.5}Al_{0.5}$-500d	6.01	350#			10	3	3	35	15	4	4	45
C−$Co_2Fe_{0.5}Al_{0.5}$-600		22#			4	18	1	8	11	50	3	6
C−$Co_2Fe_{0.5}Al_{0.5}$-600d	6.21	143	18	125	23	16	14	37	15	10.5	11	20
C−Ni_2Al-500	5.90	8.5#			1.5	18	0.5	3	4	47	0	15
C−Ni_2Al-500d	5.22	31	12	19	13	42	3	53	42	135.5	1	319
C−Ni_2Al-600	6.43	62#			5	8	2	15	5	8	3	6
C−Ni_2Al-600d	4.89	428	227	201	27	6	28	30	39	9	31	35

[a] D/G corresponds to the carbon in-plane coherence domain evaluated by Raman spectroscopy (see text). [b] Data obtained from N_2 adsorption; S is the specific surface area calculated using the BET method and *t*-plot for the microporous surface contribution (S_μ) and the external surface (S_T). The pound symbol (#) denotes data obtained from a 10-point adsorption analysis). [c] Capacitance calculated using cyclic voltammetry at a scan rate of 2 mV/s. [d] Outer charge q_0*, defined as the charge on the most accessible active surface, obtained by extrapolation of q* to $v = \infty$ from the q* vs $v^{-0.5}$ plot. [e] Total charge q_T*, defined as the charge related to the entire electrochemically active surface, obtained by extrapolation of q* to $v = 0$ from the q* vs $v^{0.5}$ plot.

3.3. Acid-Leaching Treatment: Carbon Composite and Carbon Replica. Samples treated at the selected temperatures of 500 and 600 °C present some crystalline products (see Figure 3) that were identified as ZnO, ZnS, Co (JCPDS File Card No. 15-0806), Co_8FeS_8, $FeAl_2O_4$ (JCPDS File Card No. 34-0192), $CoFe_2O_4$, CoO, Ni, NiO, NiS, and Ni_3S_2 (JCPDS File Card No. 44-1418). These phases appear at different temperatures. Indeed, inorganic residual compounds are present after the thermal treatment at 500 °C and still remain with others at 600 °C. Evidently, there is a dependence of the thermal treatment on the crystallinity of the residual inorganic compounds. Indeed, the byproducts are more crystallized at higher temperature, and the diffraction peaks become narrower, as exemplified with ZnO. An acid-leaching treatment in an acidic medium is necessary to obtain a carbon replica without inorganic residual compounds. However an acid-leaching treatment using 5 M HCl, in some cases, causes only partial demineralization. For a carbon composite carbonized at 500 °C, the acid leaching is rather efficient and only a trace of NiO is observed for C−Ni_2Al-500d. In contrast, after a carbonization at

600 °C, which favors greater crystallinity, $ZnAl_2O_4$ is observed for C−Zn_2Al-600d, as well as $FeAl_2O_4$ for C−$Co_2Fe_{0.5}Al_{0.5}$-500d. $FeAl_2O_4$ is observed to be stable in an acid medium, because it is retrieved after acid leaching, while $ZnAl_2O_4$, which is absent from the carbon composite, is formed during the acid leaching, supposedly by the consumption of the ZnO, which is unstable in an acidic medium, to form with dispersed Al^{3+} cations, the spinel stable in acid. Similarly, the selective acid leaching was used to generate porous dense framework taking advantage of the stability against dissolution of multiphase system in an acidic medium.[46b,58] Such discriminative leaching using selective solid extraction may be of interest, but its optimization is beyond the scope of the present work.

SEM images (see Figure 4, SEI-4) is recorded before and after the acid-leaching treatment, thus underlining the role of such treatment. After the thermal treatment, the carbon composites exhibit a texture composed of grains, crystals of small dimension embedded into a carbon matrix. Residual inorganic compounds are determined to be rather dispersed in a homogeneous way. In agreement with *ex situ* XRD analysis, the apparent size of the crystallized byproduct increases with the temperature of carbonization. The residual inorganic compounds disappear after the acidic treatment and a continuous porous texture is then observed. Such an observation is consistent with the fact that the inorganic small particles are acting as pore formers.

The carbon composite and replica (i.e., before and after acid leaching) are characterized by Raman and ESR spectroscopy. Raman spectra consist of the two well-known peaks centered on 1360 and 1600 cm^{-1} (SEI-5), and attributed to D and G carbon contribution, respectively.[59] The broad band labeled G corresponds to the E_{2g} symmetric vibrational mode of graphite-type sp^2 carbon, while D is an indicator of structural disorder level characterized by the bond angle distribution and linking with sp^3 carbons. The relative intensity of D over G Raman contribution is calculated to provide the microcrystalline planar size L_a of carbon-related materials according to $I_D/I_G = 4.4/L_a(\text{nm})$.[59c,d] The values are summarized in Table 2 and are in the range 4.4 nm $< L_a <$ 7.7 nm, thus underlining the presence of a relatively high degree of disorder. Even if a general trend against the LDH nature, carbonization temperature and acid-leaching process is here difficult to rationalize, the values are however greater than the results obtained from styryl organo-modified Zn_2Al for carbon replica obtained in similar conditions ($L_a < 2.5$ nm),[31a] showing that the nature of the carbon source is one of the major parameters governing L_a.

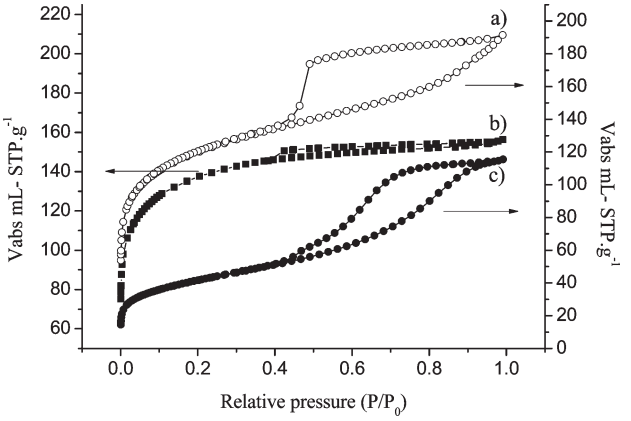

Figure 5. N_2 adsorption−desorption isotherms for different carbon replicas: (a) C−Zn_2Al-500d, (b) C−Ni_2Al-600d, and (c) C−$Co_2Fe_{0.5}Al_{0.5}$-600d.

As previously observed,[31b] the ESR signals of the carbon replicas are composed of contributions of different peak-to-peak linewidths; however, all of them are assigned to carbonaceous radicals (Landé splitting factor *g*-value of 2.004) (SEI-6). The narrow line is attributed to σ-radicals (dangling bonds), whereas the broader line is characteristic of aromatic π-radicals.[60] Interestingly, it is found that, in comparison to carbon replicas of AMPS issued after treatment at 500 °C, the sequestration results in a strong decrease in the spin density, from 172.0×10^{17} spin/g down to 87.1×10^{17} spin/g (using Zn_2Al), 19.4×10^{17} spin/g (using Ni_2Al), and 15.1×10^{17} spin/g (using $Co_2Fe_{0.5}Al_{0.5}$). ESR measurements on the carbon composites were not performed.

The textural properties of the carbon replica are evaluated by means of N_2 adsorption. The data are gathered in Table 2 and are exemplified for the three different LDH matrices in Figure 5. After calcinations at either 500 or 600 °C, but before the acid-leaching procedure, the carbon composites present rather low specific surface areas (as evaluated via the BET method). It is exemplified here by C−$Co_2Fe_{0.5}Al_{0.5}$-500 and C−$Co_2Fe_{0.5}Al_{0.5}$-600, presenting specific surface areas of 95 and 22 m^2/g, respectively. At this step, the samples are composed from aggregations of different particles of increasing size, relative to temperature, and are embedded into a carbon matrix. After acid leaching, a steep rise in the adsorption curve ($V-(P/P_0)$) is occurring in the low relative pressure range. This is characteristic of the presence of micropores. A deviation in the absorption curve is depicted above $P/P_0 = 0.1$ (i.e., above the monolayer formation), where the change in curvature is indicative of a sorption uptake at the external surface and is measured by S_T (Table 2). Depending on the LDH container and, consequently, the nature and crystallinity of the byproduct, a trend is not easy to disentangle. However, one may observe some major effects: (i) the variation of the specific surface area is, for the carbon replica, highly dependent on the LDH container, as well as the carbonization temperature; (ii) the relative amount of surface that comes from micropores (S_μ) is inversely proportional to

(58) Zou, L.; Li, F.; Xiang, X.; Evans, D. G.; Duan, X. *Chem. Mater.* **2006**, *18*, 5852.
(59) (a) Matthews, M. J.; Dresselhaus, M. S.; Endo, M.; Sasabe, Y.; Takahashi, T.; Takeuchi, K. J. *Mater. Res.* **1996**, *11*, 3099. (b) Kostecki, R.; Tran, T.; Song, X.; Kinoshita, K.; McLarnon, K. *J. Electrochem. Soc.* **1997**, *144*, 3111. (c) Shimodaira, N.; Masui, A. *J. Appl. Phys.* **2002**, *92*, 902. (d) Reshetenko, T. V.; Avdeeva, L. B.; Ismagilov, Z. R.; Pushkarev, V. V.; Cherepanova, S. V.; Chuvilin, A. L.; Likholobov, V. A. *Carbon* **2003**, *41*, 1605.
(60) Lewis, I. C. *Carbon* **1982**, *20*, 519.

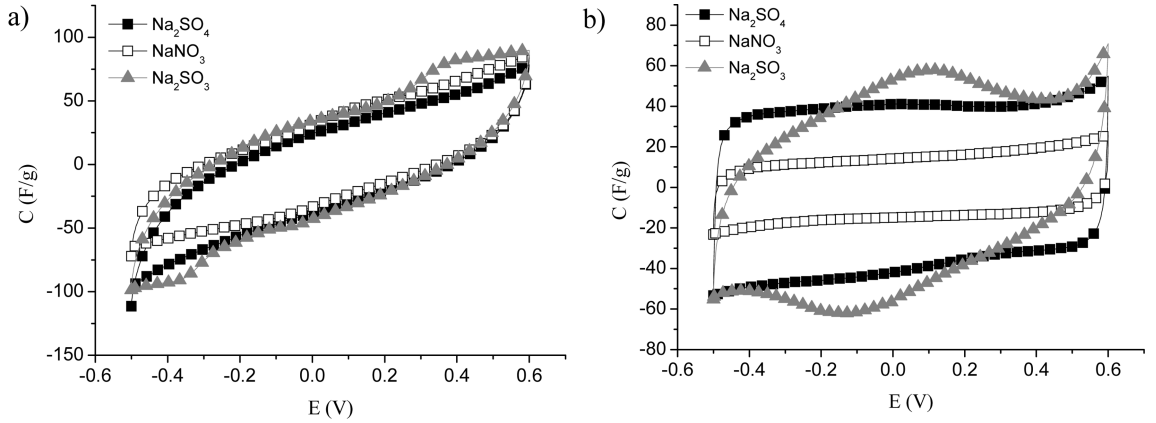

Figure 6. Cyclic voltammogram curves for (a) C−$Co_2Fe_{0.5}Al_{0.5}$-500 and (b) C−$Co_2Fe_{0.5}Al_{0.5}$-600d at a scan rate of 2 mV/s. The electrolyte salt is indicated.

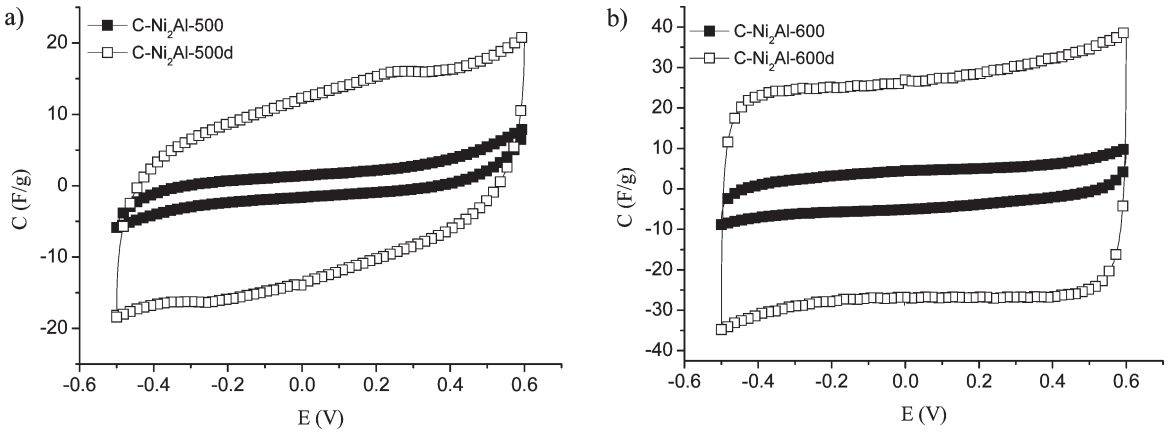

Figure 7. Cyclic voltammogram curves at a scan rate of 2 mV/s, using 0.5 M Na_2SO_4, as a function of acid leaching for a carbonization temperature of (a) 500 °C and (b) 600 °C for a Ni_2Al/AMPS hybrid precursor.

the crystallinity of the byproduct that remains in the carbon replica (for a carbonization temperature of 600 °C); and (iii) similarly, an increase in the crystallinity of the inorganic particles decreases the specific surface area of the carbon composite.

For instance, items (i) and (ii) are nicely illustrated by C−Ni_2Al-500d and C−Ni_2Al-600d, because the latter presents an open porosity concomitantly with an absence of the byproduct, whereas the former presents a rather small porosity with the presence of NiO. Similarly, but inversed with regard to temperature, C−Zn_2Al-500d presents a greater specific surface area and associated S_μ value than C−Ni_2Al-600d; a crystallized byproduct is absent for the former, whereas $ZnAl_2O_4$ is observed for C−Zn_2Al-600d (see Figure 3).

One should note that, here, the specific surface area generated by the LDH sequestration is always higher than that observed in the absence of an LDH container. However, here, the values obtained by the replica process are relatively small, much smaller than that observed in the case of other comparative systems, such as the styryl LDH hybrid-type assembly.[30,31a]

3.4. Electrochemical Behavior. Even if a large specific surface area, which is usually required for EDLC,[61] is not observed here, the capacitive behavior is, however, characterized in different aqueous electrolytes by cyclic voltammetry. In addition to the salts commonly used in aqueous electrolytes (KOH[61] and Na_2SO_4),[62] $NaNO_3$ and Na_2SO_3 are also considered to promote the pseudocapacity. Indeed, the formation of EDL is highly dependent on the interface between the electrode functionalized surface and the electrolyte salt. For instance, Co_xNi_{1-x} LDH material has exhibited one of the highest values for oxide materials in 6 M KOH,[52] whereas the performance of Fe_3O_4 as a supercapacitor is optimized using the electrolyte salt Na_2SO_3 against Na_2SO_4 or KOH.[63]

Before acid leaching, the carbon composites exhibit a strong pseudo-capacitive behavior (see Figure 6a), regardless of the electrolyte, and are associated with a rather low capacitance, because the utmost value was 40 F/g for C−$Co_2Al_{0.5}Fe_{0.5}$-500. The other carbon

(61) Raymundo-Pinero, E.; Kierzek, K.; Machnikowski, J.; Beguin, F. *Carbon* **2006**, *44*, 2498.

(62) (a) Toupin, M.; Brousse, T.; Belanger, D. *Chem. Mater.* **2004**, *16*, 3184. (b) Athouël, L.; Moser, F.; Dugas, R.; Crosnier, O.; Belanger, D.; Brousse, T. *J. Phys. Chem. C* **2008**, *112*, 7270.

(63) (a) Zhang, Z. J.; Chen, X. Y.; Wang, B. N.; Shi, C. W. *J. Cryst. Growth* **2008**, *310*, 5453. (b) Wang, S. Y.; Ho, K. C.; Kuo, S. L.; Wu, N. L. *J. Electrochem. Soc.* **2006**, *153*, A75.

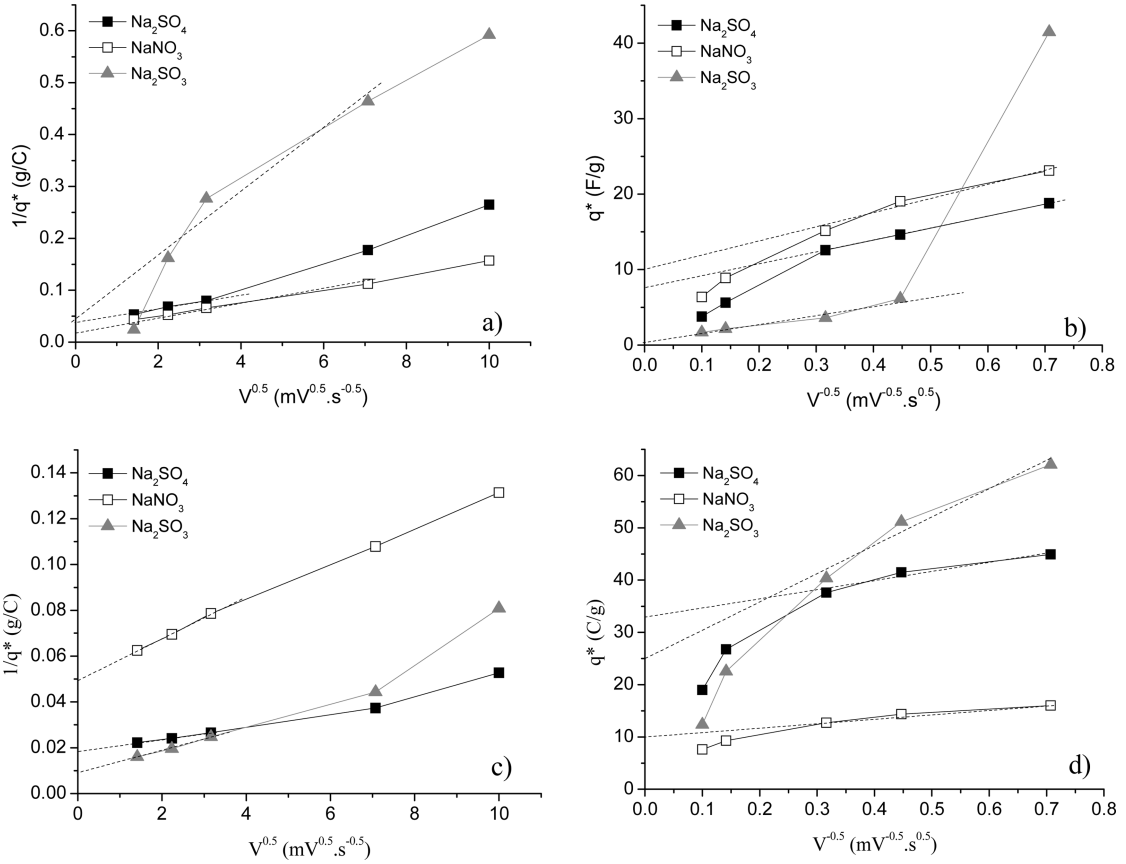

Figure 8. Variation of the voltammetric charge q^* (expressed in units of C/g), with respect to the sweep rate v (given in units of mV/s), expressed as (panels a and c) q^{*-1} vs $v^{1/2}$ and (panels b and d) q^* vs $v^{-1/2}$ for C−$Co_2Fe_{0.5}Al_{0.5}$-500 (panels a and b), and C−$Co_2Fe_{0.5}Al_{0.5}$-600d (panels c and d).

composites exhibit much lower capacitance (< 5 F/g), and an increase in the carbonization temperature from 500 °C to 600 °C induces a strong decrease of the capacitance. Inherent to the rather small specific surface area, this corresponds to C−$Co_2Al_{0.5}Fe_{0.5}$-500, which has a capacitance per surface unit of ∼50 μF/cm^2; this value is greater than what should be expected from true EDLC.[31c] Therefore, such behavior is explained by pseudo-capacitance, which ranges in the following order:$NaNO_3 > Na_2SO_4 > Na_2SO_3 >$ KOH.

Such an oblique $I-V$ response is changed to a bumped-shaped rectangular form after acid leaching (Figure 6b), and the anodic-to-cathodic charge ratio is now ∼1, typical of a condenser-like interface. An increase in the carbonization temperature improves the capacitance, and values of ∼65 F/g are attained for C−Ni_2Al-600d in KOH (6 M), corresponding to 15 μF/cm^2. C−Ni_2Al-500d with a specific surface area of ∼31 m^2/g presents a specific capacitance per surface unit of 135 μF/cm^2 in $NaNO_3$; again, this value is much higher than that expected from a true EDLC. The electrochemical response in Na_2SO_3 is quite different, because the cathodic and anodic sweeps present a hump that is reversible during cycling. The effect of both the carbonization temperature and acid leaching is clearly evidenced on the voltammograms for C−Ni_2Al-based carbon composite and replica in Na_2SO_4 (see Figure 7). It is interesting to note, in the absence of an LDH container, that the capacitive response before or after acid leaching is very low and does not exceed 10 F/g, regardless of the nature of the salt (see Table 2), demonstrating the substantial benefit of the LDH sequestration.

Additional information may be obtained from the response obtained by varying the potential scan rate, as exemplified by C−$Co_2Al_{0.5}Fe_{0.5}$-500 and C−$Co_2Al_{0.5}Fe_{0.5}$-600d in Na_2SO_3 displayed in Figure 8. This phenomenological approach was initially used to probe the surface of a mixed oxides electrode[64] and was recently applied to electrochemical systems as diverse as α-MnO_2 cryptomelane[65] and nanocrystalline $Ti_xFe_yRu_ZO_n$.[66] As observed in these systems, the voltammetric charge response is observed to decrease as the potential scan rate increases. The total charge (q_T*), which is proportional to the entire active surface, is obtained from extrapolation of q^* to $v = 0$ on a plot of q^{*-1} vs $v^{1/2}$ (see Figures 8a and 8c), whereas the outer charge (q_0*), which is proportional to the outer active surface, is extrapolated from the $q^*-v^{-1/2}$ curve (see Figures 8b and 8d). Both plots are more or less satisfactorily linear over the entire tested range of v (the deviation will be discussed in the following examination), and q_T* and q_0* are then listed in Table 2. The difference between the two limiting charges results in the charge

(64) (a) Ardizzone, S.; Fregonara, G.; Trasatti, S. *Electrochim. Acta* **1990**, *35*, 263. (b) De Pauli, C. P.; Trasatti, S. *J. Electroanal. Chem.* **1995**, *396*, 161.
(65) Toupin, M.; Brousse, T.; Belanger, D. *Chem. Mater.* **2002**, *14*, 3946.
(66) Soudan, P.; Gaudet, J.; Guay, D.; Belanger, D.; Schulz, R. *Chem. Mater.* **2002**, *14*, 1210.

related to the inner active surface (q_i*) by the relation $q_T^* = q_0^* + q_i^*$

For the carbon replica, an increase in the carbonization temperature decreases the relative part of q_0* vs q_T* and for C−Ni_2Al-600d $q_0^* = q_T^*$ (in Na_2SO_4 and $NaNO_3$) showing the quasi-absence of "inner" site, the material is then fully exposed (Table 2, complementary data in SEI-7). The associated "electrochemical porosity", which is defined as the ratio q_i^*/q_T^*, is ~0.1,[64b] whereas it ranges from 0.4 to 0.9 for the other carbon replicas. For the carbon composites, the situation is more complex, because extrapolation to $v \rightarrow \infty$ underestimates q_0*, because of the reversibility of the surface redox processes rapidly fading under a high scan rate. This is the reason for the rather small values that are obtained for q_0* and, consequently, an associated "electrochemical porosity" from 0.5 up to 0.95. For instance, and in opposition to C−Ni_2Al-600d, C−$Co_2Al_{0.5}Fe_{0.5}$-600d presents a total charge q_T* that is much greater than the outer charge q_0*, regardless of the nature of the salt, but with a difference that is largely enhanced in the case of Na_2SO_3 (q_0^* = 27 C/g and q_T^* = 109 C/g), which is indicative of a pronounced "inner active surface" (see Figures 9c and 9d). Similarly, for the corresponding carbon composite at 500 °C, C−$Co_2Al_{0.5}Fe_{0.5}$-500, a drastic increase in response is observed at a slow potential scan rate of 2 mV/s (see Figures 9a and 9b); however, here, this is interpreted by the presence of redox reactions (see below).

Contrary to the general pervasive idea that a greater specific surface area should result in greater capacitive properties, here, it is demonstrated that the carbon replica that develops a large specific surface, area such as C−Zn_2Al-500d presents rather low capacitive properties, while others with moderate values, such as C−$Co_2Al_{0.5}Fe_{0.5}$-600d presents interesting EDLC properties. For the carbon composite, C−$Co_2Al_{0.5}Fe_{0.5}$-500 is observed to behave quite well. Therefore, in the following, we focus our attention on both the carbon composite and the replica, C−$Co_2Al_{0.5}Fe_{0.5}$-500 and C−$Co_2Al_{0.5}Fe_{0.5}$-600d, respectively, having in mind that other carbon materials are also relevant such as C−Ni_2Al-600d.

When using Na_2SO_3, the potential stability is determined to be extended to the domain from −0.9 to +0.9 V, mostly for carbon composites (see Figure 9), thus contributing more extensively to the specific energy. When comparing $q^*-v^{-1/2}$ and $q^{*-1}-v^{1/2}$ curves, the total charge for C−$Co_2Al_{0.5}Fe_{0.5}$-600d is not modified (103 C/g versus 109 C/g), while the outer charge is largely increased from 27 C/g to 88 C/g when changing the potential window (see Figure 10). This demonstrates that the extended electrochemical reaction occurs in the EDL vicinity, thus artificially diminishing the "inner" surface, because we surmise that the wettability of the material should not be drastically modified. For the carbon composite, C−$Co_2Al_{0.5}Fe_{0.5}$-500, a drastic change is observed; q_T* increases from 20 C/g to 221 C/g and q_0* from 1 C/g to 22 C/g (see Figure 10).

Complex impedance spectroscopy is performed on the optimized samples, C−$Co_2Al_{0.5}Fe_{0.5}$-500 and

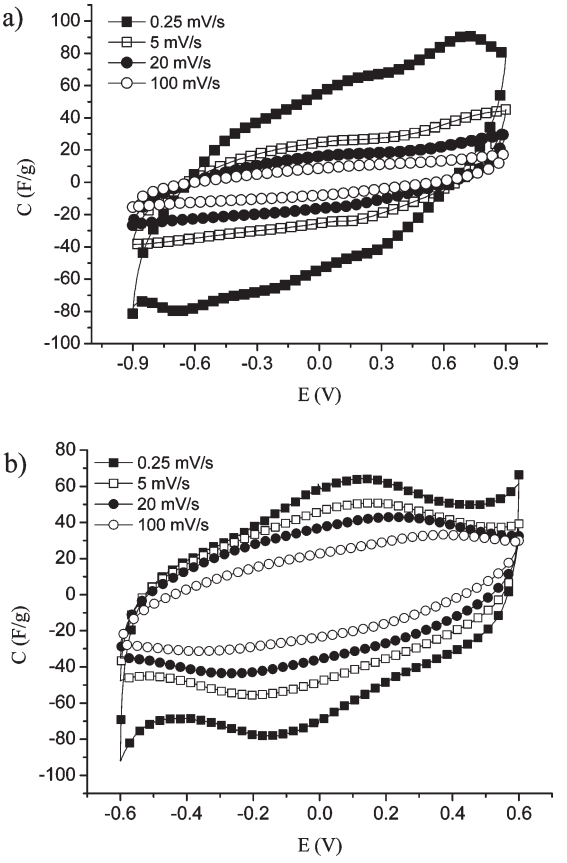

Figure 9. Cyclic voltammogram curves for (a) C−$Co_2Fe_{0.5}Al_{0.5}$-500 and (b) C−$Co_2Fe_{0.5}Al_{0.5}$-600d at different indicated sweep rates, using 1 M Na_2SO_3 in an optimized potential domain (see text).

C−$Co_2Al_{0.5}Fe_{0.5}$-600d in Na_2SO_3 at both potential limits (see Figure 11). Plotted as a Nyquist-type curve, the imaginary part of the impedance for C−$Co_2Al_{0.5}Fe_{0.5}$-600d approaches a phase angle of $\pi/4$ that is deviated from an angle of $\pi/2$, which is expected from true capacitive behavior. This can be explained by the pseudo-capacitive response of the carbon replica, as well as by the roughness of the electrolyte/material interface that was not further optimized. The intercept of the dashed lines to the Z'-axis corresponds to the equivalent serial resistance (ESR) of the two-electrode capacitor (see the enlarged portion of Figure 11), which is due to the ionic resistivity of the electrolyte present in the porosity of the active material. At both potential limits, the high-frequency response is mostly superimposed, and the ESR value is ~1.96 Ω/cm^2, while the response in the low-frequency domain is shifted by a smaller phase angle in the case of −600 mV. For the carbon composite, the ESR value is much greater, and a second arc on the $Z'-jZ''$ curve is observed at lower frequency, showing that a resistive process is dominant in the corresponding time scale.

It is well-accepted that the pseudo-capacitance comes from surface redox reactions that occur rapidly. For the carbon replica, it may come from N atoms, which are well-known to present such phenomena especially in acidic electrolytes;[12] however, the linear dependence between nitrogen content and the electrochemical

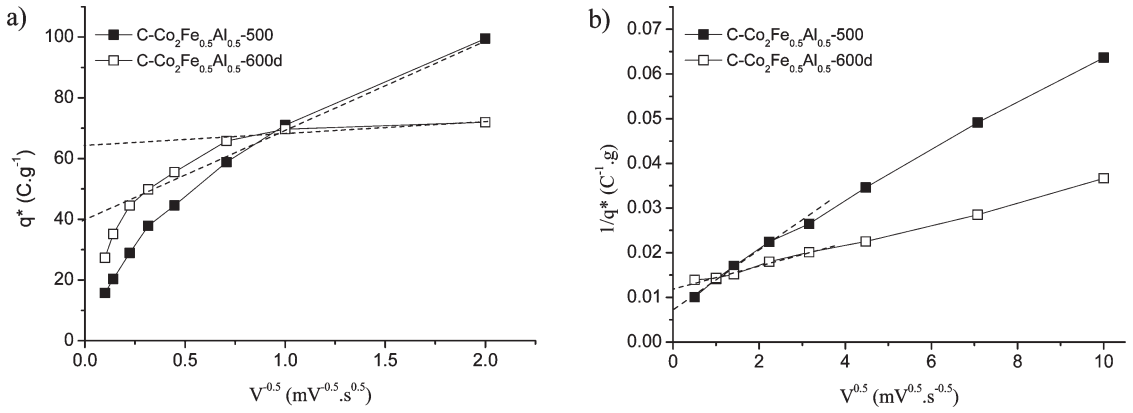

Figure 10. Variation of the voltametric charge q^* (expressed in units of C/g), with respect to the sweep rate v (in units of mV/s) expressed as (a) $q^*-v^{-1/2}$ and (b) $q^{*-1}-v^{1/2}$ for C−$Co_2Fe_{0.5}Al_{0.5}$-500 and C−$Co_2Fe_{0.5}Al_{0.5}$-600d under the operating conditions described for Figure 9.

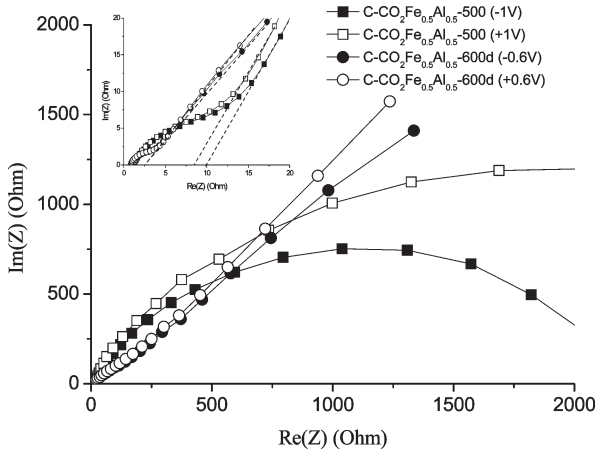

Figure 11. Complex plane impedance expressed as $Z'-jZ''$ Nyquist curves for C−$Co_2Fe_{0.5}Al_{0.5}$-500 and C−$Co_2Fe_{0.5}Al_{0.5}$-600d at imposed potentials. Low impedance domain is enlarged in the inset and the ESR is indicated by a dashed line.

capacitance is somehow controversial.[50,67] We surmise that similar reactions may occur at neutral pH, also involving other nitrogen-based end-capped functions. In addition, the extension of the voltage domain allows some chemical reactions to occur, according to

$$SO_3^{2-} + 2OH^- \leftrightarrow SO_4^{2-} + H_2O + 2e^- \quad (E = -0.93 \text{ V vs SHE}) \qquad (1)$$

$$2SO_3^{2-} + 3H_2O + 4e^- \leftrightarrow S_2O_3^{2-} + 6OH^- \quad (E = -0.57 \text{ V vs SHE}) \qquad (2)$$

where reactions 1 and 2 may occur in oxidation and in reduction, respectively. Others may happen in cascade, such as

$$2S_2O_3^{2-} \leftrightarrow S_4O_6^{2-} + 2e^- \ (E = 0.08 \text{ V vs SHE}) \qquad (3)$$

Indeed, and as explained by other authors,[63b] additional pseudo-capacitance may come from a cascade reaction of specifically adsorbed sulfite anions, thus forming a double layer that, electrochemically, is more active. From an electrochemical quartz-crystal microbalance analysis along with cyclic voltammetry, the authors observe a mass increase during cathodic sweep that they explain via reaction 2, as well as by another consecutive reaction:

$$S_2O_3^{2-} + 3H_2O + 8e^- \leftrightarrow 2S^{2-} + 6OH^- \qquad (4)$$

At a first glance, the additional contribution when cycling within a larger potential domain should be of true EDLC-type response coming from favorable specific adsorption site but one cannot discard also a contribution as ion pair acting as electron shuttle for the possible redox reaction. The latter phenomenon was observed in the case of enhanced capacitive properties of CoAl-based LDH, in the presence of $Fe(CN)_6^{3-}/Fe(CN)_6^{4-}$, where such an additive in the electrolyte was determined to facilitate the electron transfer, because the charge-transfer resistance decreases at all applied potentials, while the double-layer characteristics are maintained.[68]

From the results displayed in Figure 10, it is demonstrated that the additional shuttle ion effect benefits the pseudo-capacitive response, as long as the potential sweep is performed on the larger potential domain, and carbon composites then contribute more from the additional capacitance than the carbon replicas, because of their respective stability. However, in terms of preliminary performance, an electric energy of 39.5 W s/g ≡ 11.0 W h/kg that is associated with a power density of 87.75 kW/kg, however, is retrieved for C−$Co_2Al_{0.5}Fe_{0.5}$-600d on ΔV = 1.2 V, using a potential scan rate of 2 mV/s, making it an interesting possible candidate as a capacitor in an aqueous electrolyte. For the carbon composites, other reactions coming from the inorganic byproduct may also occur as some inorganic solids are exposed to react electrochemically, as exemplified by C−$Co_2Al_{0.5}Fe_{0.5}$-500 with small crystallites of $FeAl_2O_4$ (see Figure 3).

Indeed, a fully exposed electroactive site is a benefit for redox capacitors,[52,53] but it also is evident that such exposure is an advantage to electron transfer into bulk. As depicted in Figure 10, slower scan rates v substantially

(67) Hulicova, D.; Yamashita, J.; Soneda, Y.; Hatori, H.; Kodama, M. *Chem. Mater.* **2005**, *17*, 1241.

(68) Su, L. H.; Zhang, X. G.; Mi, C. H.; Gao, B.; Liu, Y. *Phys. Chem. Chem. Phys.* **2009**, *11*, 2195.

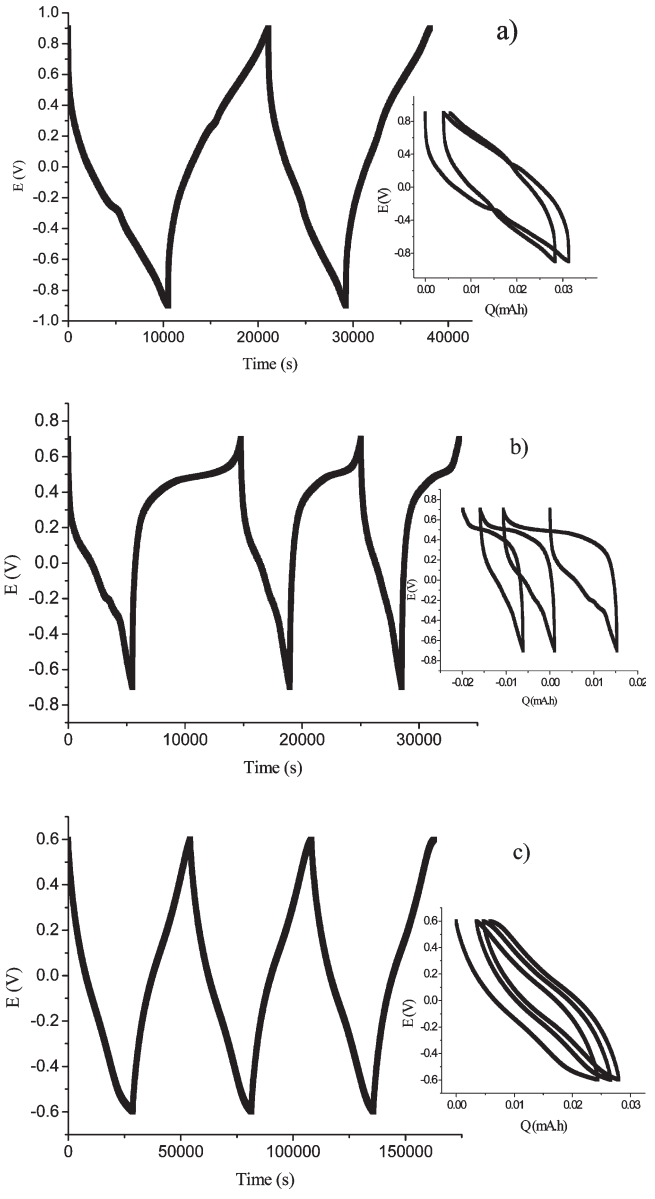

Figure 12. Galvanostatic curve E(V)$-t$(s) for (a) C$-Co_2Fe_{0.5}Al_{0.5}$-500, (b) C$-Co_2Fe_{0.5}Al_{0.5}$-600 and C$-Co_2Fe_{0.5}Al_{0.5}$-600d, using a current density of 11, 12, and 5 mA/g (reported to the total electrode mass). Inset shows the corresponding variation E(V) vs Q(mAh).

increase the response of carbon composites, and several humps are visible for $v = 250$ μV/s. To access the Coulombic efficiency, the galvanostatic mode is applied. C$-Co_2Al_{0.5}Fe_{0.5}$-500 is cycled in the potential domain from -0.9 V to $+0.9$ V with a current of 11 mA/g (reported per total electrode mass) (see Figure 12a). In this mode, a linear response $V-t$ is characteristic of capacitance (a plateau in $I-t$), whereas a plateau here is indicative of a redox reaction (a hump in the $I-t$) plot. The total response is of 88 F/g, which is much greater than that obtained at 2 mV/s (33 F/g); this suggests the presence of reversible redox reaction occurring at the slow regime. Taking into account the molecular weight of C$-Co_2Al_{0.5}Fe_{0.5}$-500 calculated from TGA (given as $M_w = 269.5$ g/mol), the obtained specific capacity of $\sim$43 mAh/g corresponds to a Coulombic titration of $\Delta e^-/M_w \approx 0.6$. Similarly, C$-Co_2Al_{0.5}Fe_{0.5}$-600 displays a

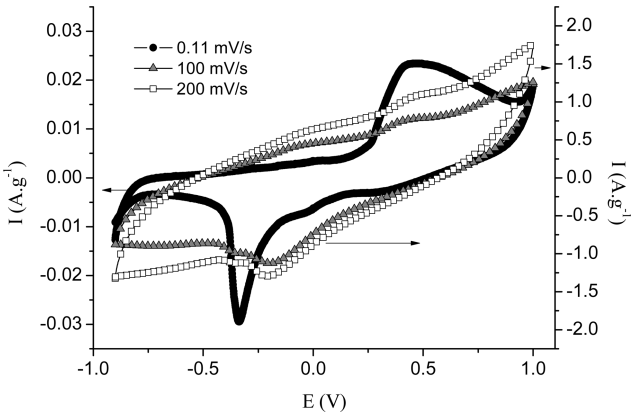

Figure 13. Cyclic voltammogram curves for an asymmetric cell composed of C$-Co_2Fe_{0.5}Al_{0.5}$-500 and C$-Co_2Fe_{0.5}Al_{0.5}$-600 at different indicated sweep rates using 1 M Na_2SO_3 in optimized potential domain (see text).

reversible specific capacity of 22 mAh/g that is associated with some irreversible processes that occur during the cathodic sweep as the associated capacity in charge Q_C is always greater than the subsequent process Q_A, thus shifting the $V-Q$ curve on the left (Figure 12b). For comparison, the galvanostatic curve of the carbon replica C$-Co_2Al_{0.5}Fe_{0.5}$-600d is displayed in Figure 12c. The Coulombic titration for C$-Co_2Al_{0.5}Fe_{0.5}$-500 is less than that observed in the case of noncalcined LDH M^{II}/Al ($\Delta e^-/M_w$ of $\sim$1).[69] It is arising from different electrochemical mechanisms, and the electrochemical performances reported by mass here are much lower due to the electronically conductive carbon part that is ensuring the capacitive high-regime response.

The electrochemical features obtained from the $V-Q$ curve are quite different between C$-Co_2Al_{0.5}Fe_{0.5}$-500 and C$-Co_2Al_{0.5}Fe_{0.5}$-600 (see Figures 12a, 12b, and inset). The first carbon composite presents a sloppy reversible curve, whereas the second gives a defined plateau during the cathodic sweep. An asymmetric cell, using C$-Co_2Al_{0.5}Fe_{0.5}$-600 as the positive electrode and C$-Co_2Al_{0.5}Fe_{0.5}$-500 as the negative electrode, is presented in Figure 13. The asymmetric system is often used in supercapacitor systems, because the negative electrode usually requires large accessibility, and the performance is governed by the pore size distribution of the carbon used in the negative electrode.[70] Preliminary results show that the asymmetric cell system cycles from the low regime (0.11 mV/s) to fast (200 mV/s), thus demonstrating dual electrochemical properties, EDLC type as well as specific capacity, which is rather well-balanced between the anodic sweep ($C_A = 60$ F/g) and cathodic sweep ($C_C = 94$ F/g) in the slow regime. Such an asymmetric cell is reminiscent of the rocking-chair lithium-ion system studied in an aqueous electrolyte using $LiMn_2O_4/VO_2$

(69) (a) Sugimoto, A.; Ishida, S.; Hanawa, K. *J. Electrochem. Soc.* **1999**, *146*, 1251. (b) Caravaggio, G. A.; Detellier, C.; Wronski, Z. *J. Mater. Chem.* **2001**, *11*, 912. (c) Mavis, B.; Akinc, M. *J. Power Sources* **2004**, *134*, 308. (d) Casas-Cabanas, M.; Rodriguez-Carvajal, J.; Canales-Vazquez, J.; Palacin, M. R. *J. Mater. Chem.* **2006**, *16*, 2925.

(70) Wang, L.; Morishita, T.; Toyoda, M.; Inagaki, M. *Electrochim. Acta* **2007**, *53*, 882.

and $LiNO_3$[71a] or LiOH[71b] as salt. Such electrochemical devices were determined to be a safe and cost-effective method, competing well with nickel−cadmium and lead-acid batteries, in terms of stored energy per weight, as long as special care of the pH value, electrolyte salt nature, and concentration were taken.[71c,d] The parameters here are also of great concern to endow the carbon portion with suitable capacitive and pseudo-capacitive properties, as well as proper operating conditions for rapid redox reactions to occur for the well-dispersed inorganic particles.

4. Concluding Remarks

The development of high-energy-density supercapacitors has been focused primarily on nanoporous carbon materials, with, recently, special attention given to the functionalized surface. However, we demonstrate here that an alternative is to consider carbon composites or replicas that are obtained after hybrid organic/inorganic layered double hydroxide (O/I LDH) carbonization and acid leaching, respectively. Indeed, they are observed to exhibit interesting electrochemical characteristics as supercapacitors from the slow regime to the fast regime, as long as a good compromise between carbon formation and the formation of inorganic byproduct (i.e., carbonization temperature) is met.

Effective in producing carbon nanotubes[72] and nanofibers[73] by selective reduction of mixed oxides, here, we demonstrate that the uniform distribution of the metal cations at an atomic level supplied by the LDH brucite-like layers may also result in carbon materials from O/I assembly where the inorganic byproduct may be nicely dispersed and exposed at moderate temperature, which may act as redox centers for the carbon composite or as a porogen agent for the carbon replica. We further demonstrate also that the choice of electrolyte is of great interest to expand both electrochemical double-layer capacitor (EDLC)-type behavior and the redox extended reaction. Further investigations are needed to better understand the mechanisms responsible for the redox reactions, and also to optimize the performance through a more finely tuned carbonization temperature, as well as better electrode material exposure. However, we surmise that this original concept may be applied to other cations, such as Mn and Fe,[74] which are intimately mixed at a nanometric scale with an environmentally friendly carbon source or biomass such as seaweed. Studied as a supercapacitor,[75] some of them have even been incorporated into the LDH interlayer domain.[76]

Acknowledgment. The authors would like to thank Pr. Marc Dubois (LMI), Elodie Petit (LMI), Joël Cellier (LMI), and Anne-Marie Gélinaud (Casimir, Aubière, France) for their help in acquiring the ESR, Raman spectra, in situ XRD, and SEM pictures, respectively.

Supporting Information Available: This material is available free of charge via the Internet at http://pubs.acs.org.

(71) (a) Li, W.; Dahn, J. R.; Wainwright, D. S. *Science* **1994**, *264*, 1115. (b) Li, W.; McKinnon, W. R.; Dahn, J. R. *J. Electrochem. Soc.* **1994**, *141*, 2310. (c) Zhang, M.; Dahn, J. R. *J. Electrochem. Soc.* **1996**, *143*, 2730. (d) Li, W.; Dahn, J. R. *J. Electrochem. Soc.* **1995**, *142*, 1742.
(72) (a) Li, F.; Tan, Q.; Evans, D. G.; Duan, X. *Catal. Lett.* **2005**, *99*, 151. (b) Zhao, Y.; Liang, J.; Zhou, X. J. *Adv. Mater.* **2005**, *37*, 11–15.
(73) (a) Naghash, A. R.; Xu, Z.; Etsell, T. H. *Chem. Mater.* **2005**, *17*, 815. (b) Xiang, X.; Hima, H. I.; Wang, H.; Li, F. *Chem. Mater.* **2008**, *20*, 1173.
(74) Kuo, S. L.; Wu, N. L. *Electrochem. Solid State Lett.* **2007**, *10*, A171.
(75) (a) Raymundo-Piñero, E.; Leroux, F.; Beguin, F. *Adv. Mater.* **2006**, *18*, 1877. (b) Raymundo-Piñero, E.; Cadek, M.; Beguin, F. *Adv. Funct. Mater.* **2009**, *19*, 1032.
(76) (a) Darder, M.; Lopez-Blanco, M.; Aranda, P.; Leroux, F.; Ruiz-Hitzky, E. *Chem. Mater.* **2005**, *17*, 1969. (b) Leroux, F.; Gachon, J.; Besse, J. P. *J. Solid State Chem.* **2004**, *177*, 245.